The impact of line-of-sight structures on measuring H_0 with strong lensing time delays

Nan Li [1,2]★ Christoph Becker[3] and Simon Dye [1]

[1]*School of Physics and Astronomy, University of Nottingham, University Park, Nottingham NG7 2RD, UK*
[2]*National Astronomical Observatories, Chinese Academy of Sciences, A20 Datun Road, Beijing 100012, China*
[3]*Institute for Computational Cosmology, Department of Physics, Durham University, South Road, Durham DH1 3LE, UK*

ABSTRACT

Measurements of the Hubble–Lemaitre constant from early- and local-Universe observations show a significant discrepancy. In an attempt to understand the origin of this mismatch, independent techniques to measure H_0 are required. One such technique, strong lensing time delays, is set to become a leading contender amongst the myriad methods due to forthcoming large strong lens samples. It is therefore critical to understand the systematic effects inherent in this method. In this paper, we quantify the influence of additional structures along the line of sight by adopting realistic light-cones derived from the cosmoDC2 semi-analytical extragalactic catalogue. Using multiple-lens plane ray tracing to create a set of simulated strong lensing systems, we have investigated the impact of line-of-sight structures on time-delay measurements and in turn, on the inferred value of H_0. We have also tested the reliability of existing procedures for correcting for line-of-sight effects. We find that if the integrated contribution of the line-of-sight structures is close to a uniform mass sheet, the bias in H_0 can be adequately corrected by including a constant external convergence κ_{ext} in the lens model. However, for realistic line-of-sight structures comprising many galaxies at different redshifts, this simple correction overestimates the bias by an amount that depends linearly on the median external convergence. We therefore conclude that lens modelling must incorporate multiple-lens planes to account for line-of-sight structures for accurate and precise inference of H_0.

Key words: gravitational lensing: strong – cosmological parameters.

1 INTRODUCTION

The Hubble–Lemaitre constant, H_0, is a cornerstone of the standard cosmological model, setting the distance scale, age, and critical density of the Universe. Accurate estimation of the value of H_0 is therefore critical for constraining cosmological models in the era of precision cosmology. However, presently, there is a significant mismatch between H_0 determined from early- and late-Universe probes (Riess 2019; Verde, Treu & Riess 2019), for instance, measurements of the cosmic microwave background (CMB; see Bennett et al. 2013; Planck Collaboration VI 2020) and baryon acoustic oscillations (BAO; see Addison et al. 2018; DES Collaboration et al. 2020) and those made in the more local Universe using supernovae (SNe; see Dhawan, Jha & Leibundgut 2018; Macaulay et al. 2019), the tip of the red giant branch (TRGB; see Freedman et al. 2019; Yuan et al. 2019), and Cepheid variables (Pietrzyński et al. 2019; Riess et al. 2019). Independent from any of the aforementioned methods, strong lensing time delays provide valuable measurements of H_0 (e.g. Shajib et al. 2020; Wong et al. 2020) that may assist in the understanding of these discrepancies once systematic uncertainties in the technique are fully calibrated. With such systematics in mind, in this paper we focus on the effects of line-of-sight structure, one of the most dominant sources of error in the lens time-delay method.

Strong lensing time delays are observed when a variation in flux of a strongly lensed background source such as a quasar, SN, or a gravitational wave event is detected at different times between its multiple images. The deflection of the light path from the source due to the gravitational potential of a lens, as well as the structures along the line of sight, leads to both a geometrical and a gravitational delay of the arrival time of the light from the source. The geometrical delays are sensitive to H_0 (see Schneider, Ehlers & Falco 1992). Therefore, measuring the time delays and reconstructing the mass distribution of the lens accurately allow H_0 to be estimated. The existing relative paucity of strong lens systems suitable for this method and the necessary long monitoring campaigns have somewhat limited the use of this technique but good progress has already been made with only a handful of systems (e.g. Suyu et al. 2010, 2013; Birrer, Amara & Refregier 2016; Bonvin et al. 2017; Wong et al. 2017, 2020; Chen et al. 2019; D'Agostino & Nunes 2020). However, this is set to dramatically change (Oguri & Marshall 2010; Collett 2015) with the advent of the Rubin Observatory Legacy Survey of Space and Time[1] (LSST), which will give rise to about 400 well-measured time-delay systems to constrain H_0 to within only a few per cent (Dobler et al. 2015; Liao et al. 2015).

Even with precise time-delay measurements, the reliability of estimates of H_0 depends on how faithfully the lens mass model

★ E-mail: nan.li@nottingham.ac.uk

follows the true lensing mass. Degeneracies and inadequacies in the parametrization of the lens mass model can directly propagate into the inferred value of H_0 (e.g. see Schneider & Sluse 2013; Sereno & Paraficz 2014; Xu et al. 2016; Muñoz & Kamionkowski 2017; Tagore et al. 2018; Tie & Kochanek 2018; Wagner 2018; Wertz, Orthen & Schneider 2018) as can selection effects within the lens sample (see Collett & Cunnington 2016). In addition, perturbative effects from substructure within the main lens and from structure along the line of sight can significantly modify time delays that can bias measurements of H_0 if not properly taken into account. One approach to account for these effects is to directly characterize perturbing structures identified in observations (e.g. Wong et al. 2011, 2018; Momcheva et al. 2015; Rusu et al. 2017; Sluse et al. 2017). Another common technique is to use external shear, γ_{ext}, and external convergence, κ_{ext}, in the lens model. By connecting cosmological simulations and real observations, an estimate of the distribution function of the amplitude of these external lensing effects can be obtained (e.g. Suyu et al. 2010, 2013; Collett et al. 2013; Greene et al. 2013; Birrer et al. 2017; Rusu et al. 2017; Tihhonova et al. 2018). However, the corrections provided by γ_{ext} and κ_{ext} are isotropic and cannot properly capture the complexity of real perturbing structures. Motivated by this, more sophisticated approaches have been developed using multiple-lens planes or approximations thereof (e.g. McCully et al. 2014, 2017; Birrer et al. 2017).

In this work, we investigate the influence of haloes along the line of sight on measurements of H_0 by using multiple-lens plane ray-tracing simulations. To obtain simulated time delays we construct the light-cone of each lens from a state-of-the-art semi-analytic model (cosmoDC2[2]; Korytov et al. 2019) based upon the large Outer Rim cosmological N-body simulation (Heitmann et al. 2019). By modelling these time delays with the same methods used for real data, we directly assess the biases introduced by line-of-sight effects and the efficacy with which these can be accounted for using external corrections such as γ_{ext} and κ_{ext}.

This paper is structured as follows. We outline the methodology used for determining strong lensing time delays in the cases of the single-lens plane and multiple-lens planes in Section 2. Details of the simulations and the process of estimating H_0 from the simulated data are given in Sections 3 and 4, respectively. We present our findings in Section 5, then conclude with a summary and discussion in Section 6. The cosmological model adopted in this paper is that used by cosmoDC2: Λ cold dark matter (ΛCDM) with $\Omega_\Lambda = 0.735$, $\Omega_M = 0.265$, and $H_0 = 71$ km s^{-1} Mpc^{-1}.

2 STRONG LENSING TIME DELAYS

In this section, we present a basic description of the theory of time delays in strong lensing systems with multiply-lensed point sources we have used in this work, for the cases of single- and multiple-lens planes. Throughout the paper, we have applied the thin lens approximation. For more details, we refer the reader to Schneider Ehlers & Falco (1999) and Narayan & Bartelmann (1996).

2.1 Time delays in single-lens planes

For the case of a lensing system with a single deflector, adhering to the thin lens approximation, one can project the three-dimensional mass distribution to a two-dimensional mass sheet normal to the line of sight from the observer to the source. The dimensionless surface

[2] https://portal.nersc.gov/project/lsst/cosmoDC2

mass density of a thin lens plane can be written as a function of the lens plane angular position vector, $\boldsymbol{\theta}$, as

$$\kappa(\boldsymbol{\theta}) = \Sigma(\boldsymbol{\theta} D_d)/\Sigma_{crit}, \tag{1}$$

with the critical surface mass density

$$\Sigma_{crit} = \frac{c^2}{4\pi G} \frac{D_s}{D_d D_{ds}}, \tag{2}$$

where D_s and D_d are the angular diameter distances from the source and lens to the observer, respectively, D_{ds} is the angular diameter distance from the lens to the source, and $\Sigma(\boldsymbol{\theta} D_d)$ is the surface mass density of the lens. The lensing potential is given by

$$\psi(\boldsymbol{\theta}) = \frac{1}{\pi} \int d^2\boldsymbol{\theta}' \kappa(\boldsymbol{\theta}') \ln |\boldsymbol{\theta} - \boldsymbol{\theta}'|, \tag{3}$$

and the deflection angle vector is given by

$$\boldsymbol{\alpha}(\boldsymbol{\theta}) = \frac{1}{\pi} \int d^2\boldsymbol{\theta}' \kappa(\boldsymbol{\theta}') \frac{\boldsymbol{\theta} - \boldsymbol{\theta}'}{|\boldsymbol{\theta} - \boldsymbol{\theta}'|^2}. \tag{4}$$

Once the deflection field at the lens plane is known, we can construct the lensing equation for a given set of source planes. For example, in the case of a single-lens plane and a single-source plane, the lensing equation is simply

$$\boldsymbol{\beta} = \boldsymbol{\theta} - \boldsymbol{\alpha}(\boldsymbol{\theta}), \tag{5}$$

where $\boldsymbol{\beta}$ is the angular source plane position vector that maps to $\boldsymbol{\theta}$ in the image plane (or, equivalently, 'lens plane' for the case of single-lens plane). Based on equation (5), ray-tracing simulations can be performed from the observer, crossing the lens plane to the source plane to produce lensed images. For extended-source-like galaxies, to create distorted lensed images, interpolation can be used in the source plane to map spatially varying surface brightness back to the image plane. However, for the point sources used in this work, one has to adopt triangle mapping and a barycentric coordinate system to solve the lensing equations numerically. Details of the approach are discussed in Section 3.3.

In the case of a single-lens plane, the delay of the arrival time of a light ray from the source to the observer is

$$\tau(\boldsymbol{\theta}, \boldsymbol{\beta}) = \frac{(1 + z_d)}{c} \frac{D_d D_s}{D_{ds}} \left[\frac{(\boldsymbol{\theta} - \boldsymbol{\beta})^2}{2} - \psi(\boldsymbol{\theta}) \right], \tag{6}$$

where z_d is the redshift of the lens. The last term in equation (6) is also known as the Fermat potential,

$$\Phi(\boldsymbol{\theta}, \boldsymbol{\beta}) \equiv \left[\frac{(\boldsymbol{\theta} - \boldsymbol{\beta})^2}{2} - \psi(\boldsymbol{\theta}) \right]. \tag{7}$$

This delay is undetectable, the true observable being the difference between the arrival time of two separate lensed images (say, image A and image B), $t_{AB} \equiv \tau_A - \tau_B$. From equation (6), the time difference can be written as

$$t_{AB} = \frac{D_{\Delta\tau}}{c} \Delta\Phi_{AB}, \tag{8}$$

where

$$D_{\Delta\tau} \equiv (1 + z_d) \frac{D_d D_s}{D_{ds}} \tag{9}$$

and

$$\Delta\Phi \equiv \Phi(\boldsymbol{\theta}_A, \boldsymbol{\beta}) - \Phi(\boldsymbol{\theta}_B, \boldsymbol{\beta}). \tag{10}$$

Note that

$$D_a(z) = \frac{c}{H_0(1 + z)} \int_0^z \frac{dz'}{E(z')}, \tag{11}$$

where

$$E(z) = \sqrt{\Omega_r(1+z)^4 + \Omega_m(1+z)^3 + \Omega_k(1+z)^2 + \Omega_\Lambda}. \quad (12)$$

These equations show that

$$t_{AB} \propto D_{\Delta\tau} \propto \frac{1}{H_0}, \quad (13)$$

and thus H_0 can be measured from t_{AB} if the mass distribution of the lens is reconstructed accurately.

2.2 Time delays in multiple-lens planes

In the case of multiple-lens planes, the lens equation must be modified to account for multiple deflections:

$$\boldsymbol{\beta} = \boldsymbol{\theta} - \sum_{i=1}^{N} \boldsymbol{\alpha}_i(\boldsymbol{\theta}_i), \quad (14)$$

where the quantities retain their definition from the single-lens plane case but now take on a subscript referring to a specific lens plane. We consider N mass distributions, each characterized by a surface mass density Σ_i, at redshift z_i, ordered such that $z_i < z_j$ for $i < j$ and such that the source has a redshift $z_s > z_N$. The physical distance, $\boldsymbol{\xi}_j$, of the intersections on the lens planes from the optic axis (i.e. the impact parameters) is then

$$\boldsymbol{\xi}_j = \frac{D_j}{D_1}\boldsymbol{\xi}_1 - \sum_{i=1}^{j-1} D_{ij}\hat{\boldsymbol{\alpha}}_i(\boldsymbol{\xi}_i), \quad (15)$$

where D_i is the angular diameter distance from the observer to each lens plane, D_{ij} (such that $i < j$) is the angular diameter distance from the ith lens plane to the jth lens plane, and $\hat{\boldsymbol{\alpha}}_i$ is the deflection angle at the ith lens plane (see Fig. 1). For simplicity, we convert the physical distance to angular positions on the sky $\boldsymbol{\theta}_i = \boldsymbol{\xi}_i/D_i$ and the deflection angles to effective movements on the sky:

$$\boldsymbol{\alpha}_i = \frac{D_{is}}{D_s}\hat{\boldsymbol{\alpha}}_i, \quad (16)$$

where D_{is} is the angular diameter distance from the ith lens plane to the source plane. By defining a factor B_{ij},

$$B_{ij} = \frac{D_{ij}D_s}{D_j D_{is}}, \quad (17)$$

equation (15) becomes

$$\boldsymbol{\theta}_j = \boldsymbol{\theta}_1 - \sum_{i=1}^{j-1} B_{ij}\boldsymbol{\alpha}_i(\boldsymbol{\theta}_i). \quad (18)$$

In particular, for $j = N + 1 = s$, $B_{is} = 1$, thus,

$$\boldsymbol{\beta} \equiv \boldsymbol{\theta}_{N+1} = \boldsymbol{\theta}_1 - \sum_{i=1}^{N} \boldsymbol{\alpha}_i(\boldsymbol{\theta}_i). \quad (19)$$

The delay of the arrival time of a deflected light path compared to a straight light path is the integral of the time difference along the line of sight through all lens planes. For instance, the time delay created by lens plane i and j is

$$\tau_{ij}(\boldsymbol{\theta}_i, \boldsymbol{\theta}_j) = \frac{1+z_i}{c}\frac{D_i D_j}{D_{ij}}\left[\frac{1}{2}(\boldsymbol{\theta}_i - \boldsymbol{\theta}_j)^2 - B_{ij}\psi(\boldsymbol{\theta}_i)\right], \quad (20)$$

where the first term is the geometric delay and the second is the gravitational delay. Replacing j with $i + 1$ and summing over all time delays gives the total time delay through the whole line of sight,

$$\tau(\boldsymbol{\theta}_1, \ldots, \boldsymbol{\theta}_N, \boldsymbol{\beta}) = \sum_{i=1}^{N} \tau_{i,i+1}(\boldsymbol{\theta}_i, \boldsymbol{\theta}_{i+1}). \quad (21)$$

Therefore, similar to the case of a single-lens plane, the time delay between two separate lensed images A and B can be given by

$$t_{AB} \equiv \tau_A - \tau_B$$
$$= \sum_{i=1}^{N} \tau_{i,i+1}(\boldsymbol{\theta}_{A,i}, \boldsymbol{\theta}_{A,i+1}) - \sum_{i=1}^{N} \tau_{i,i+1}(\boldsymbol{\theta}_{B,i}, \boldsymbol{\theta}_{B,i+1}), \quad (22)$$

which means that deflection fields, lensing potentials, and the angular positions of the intersections on the lens planes are all required for the calculation of time delays in multiple-lens plane systems. In Section 3, we discuss how we construct a light-cone and model the lenses to obtain the information required to implement time-delay simulations with multiple-lens planes.

3 SIMULATIONS

To quantify the influence of galaxies along the line of sight on measuring H_0 with strong lensing time delays, we generated simulated images following the formalism in Section 2 for both single- and multiple-lens planes with a strong lensing simulation pipeline named PICS (Li et al. 2016). In this section, we describe the simulations used and how the lens equations are solved using a triangle-mapping algorithm.

3.1 Semi-analytic light-cones

For creating light-cones with realistic spatial and redshift distributions of the galaxies, we extract light-cones from the cosmoDC2 synthetic source catalogue (Korytov et al. 2019). Designed for an LSST data challenge project, it is established upon a large cosmological simulation called the Outer Rim simulation run by the Argonne Cosmology Group using the Hybrid/Hardware Accelerated Cosmology Code (HACC; Habib et al. 2016). CosmoDC2 covers 500 deg^2 in the redshift range $0.0 \leq z \leq 3.0$ and is complete to a magnitude depth of 28 in the r band. Each galaxy is characterized by a multitude of properties including stellar mass, morphology, spectral energy distributions, broad-band filter magnitudes, host halo information, and weak lensing shear.

The light-cones for each of our strong lensing simulations are cut out from the full light-cone of cosmoDC2. Each extracted light-cone is centred on a bright central galaxy (BCG) identified in the cosmoDC2 catalogue since these massive central elliptical galaxies are likely strong lensing candidates. Each BCG forms the primary lens mass in its corresponding light-cone (see Section 3.2). The field of view of the light-cones is 20×20 arcsec^2, and the corresponding simulated images are 512×512 pixels in size. To focus on the impact of line-of-sight galaxies, we select light-cones with the primary lens located in the redshift range $z_d = 0.5 \pm 0.01$ and we assume a fixed source redshift of $z_s = 2.0$. We calculate the Einstein radius of the primary lens of each light-cone and then discard light-cones that yield Einstein radii outside the range of [1.3, 2.4 arcsec]. The lower limit avoids resolution issues encountered by ground-based telescopes/surveys [such as Canada–France–Hawaii Telescope (CFHT), Dark Energy Survey (DES), and LSST] and the upper limit discards systems that give year-like time delays. In total, we selected 500 light-cones adhering to these criteria (although this is ultimately reduced further by additional selection criteria – see the following
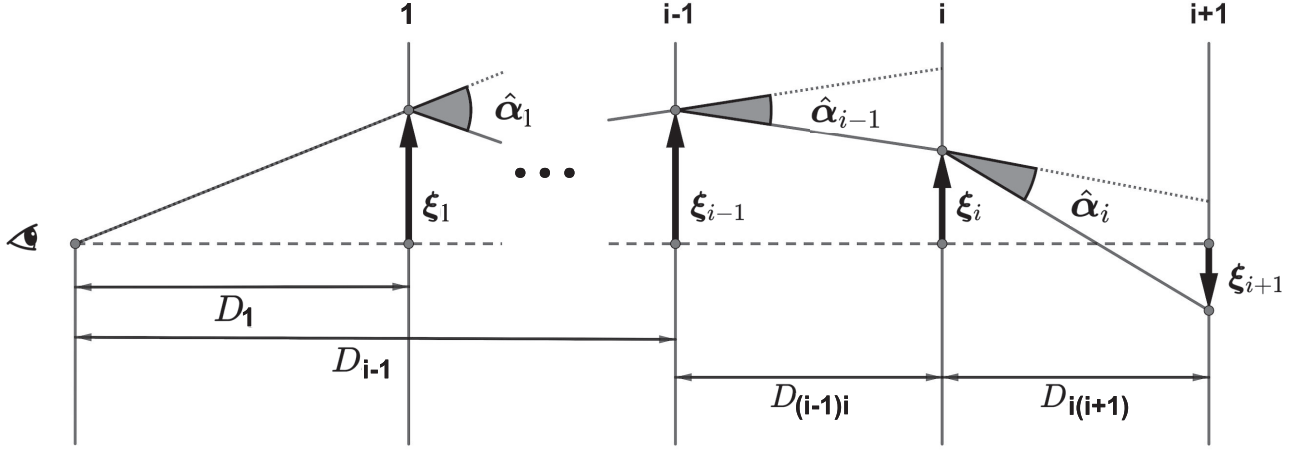
Figure 1. A schematic view of the multiplane formalism, as described in Section 2.2. A light ray (solid black line) experiences a deflection only when it passes through a lens plane (vertical solid grey lines). The deflection angle $\hat{\alpha}_i$ is the actual deflection of a ray passing through the ith lens plane, calculated from the surface density Σ_i on the ith lens plane. Using the deflection angle $\hat{\alpha}_i$ and the position of the intersection of the light ray at the $(i-1)$th lens plane, $\boldsymbol{\xi}_{i-1}$, and that at the ith lens plane, $\boldsymbol{\xi}_i$, the physical position of the intersection at the $(i+1)$th plane, $\boldsymbol{\xi}_{i+1}$, can be obtained.

section and Section 5). Furthermore, within each light-cone, we remove any deflectors with Einstein radii larger than 0.3 arcsec to concentrate our study on the effects of secondary perturbations to the lensing potential. The substructures of the primary lens are also not included so that our analysis solely concentrates on the influence of line-of-sight structures.

3.2 Ray-tracing simulations

For each light-cone, we run two sets of simulations for generating the lens time delays. The first set includes only a single-lens plane containing the primary lens galaxy. In this set, the omitted line-of-sight haloes are approximated with a constant external convergence, $\kappa_{\rm ext}$, and a constant external shear, $\gamma_{\rm ext}$, in the lens model when computing deflection angles. For each light-cone, we estimate the value of $\kappa_{\rm ext}$ and $\gamma_{\rm ext}$ by tracing multiple rays throughout it as described in more detail below. In the second set of simulations, we include all haloes in the light-cone and use a separate lens plane for each halo including the primary lens.

In both sets of simulations, we assume a singular isothermal ellipsoid (SIE) density profile for all haloes (although in our lens modelling, we use a more general elliptical power-law profile; see Section 4). The SIE profile, which provides a realistic model for the total mass profile of real elliptical galaxies (Koopmans et al. 2006; Bolton et al. 2012; Shu et al. 2016), has deflection angles given by Kormann, Schneider & Bartelmann (1994) and Keeton (2001),

$$\alpha_x \equiv \psi_x = \frac{bq}{\sqrt{(1-q^2)}} \tan^{-1}\left[\frac{\sqrt{1-q^2}\theta_x}{\phi}\right], \qquad (23)$$

$$\alpha_y \equiv \psi_y = \frac{bq}{\sqrt{(1-q^2)}} \tanh^{-1}\left[\frac{\sqrt{1-q^2}\theta_y}{\phi}\right], \qquad (24)$$

where $\phi^2 = q^2 x^2 + y^2$, q is the minor to major axial ratio, and b is an effective factor to represent Einstein radius,

$$b = \frac{4\pi}{\sqrt{q}}\left(\frac{\sigma}{c}\right)^2 \frac{D_{\rm ls}}{D_{\rm s}}. \qquad (25)$$

In the case of circular lenses, b can be calculated from the velocity dispersion. The lensing potential can be computed according to the

relationship between the lensing potential and the deflection field of SIE model (Keeton 2001),

$$\psi(\theta_x, \theta_y) = \theta_x \psi_x + \theta_y \psi_y. \qquad (26)$$

The complete parameter set required by equations (23)–(26) is $\{x_1, x_2, \sigma_v, q, \Theta, z_{\rm d}\}$, where (x_1, x_2) is the angular position of the SIE profile centre with respect to the centre of the field of view, σ_v is the velocity dispersion of the lens, q is the ellipse axial ratio, Θ is the position angle of the ellipsoid, and $z_{\rm d}$ is the redshift of the deflector. The parameters $x_1, x_2, q, \Theta, z_{\rm d}$ are taken directly from the cosmoDC2 catalogue. σ_v is derived from the L–σ scaling relation from the bright sample of Parker et al. (2007) given by

$$\sigma_v = 142\left(\frac{L}{L_\star}\right)^{(1/3)} {\rm km\,s^{-1}}, \qquad (27)$$

where $\log_{10}(L/L_\star) = -0.4({\rm mag}_r - {\rm mag}_{r\star})$, and ${\rm mag}_r$ is the apparent r-band magnitude of the galaxy given by the cosmoDC2 catalogue. We adopt the assumption in More et al. (2016) that ${\rm mag}_{r\star}$ evolves with redshift as ${\rm mag}_{r\star} = +1.5(z - 0.1) - 20.44$ (Faber et al. 2007).

Sources are described by the parameter set $\{y_1, y_2, m_{\rm s}, z_{\rm s}\}$, where (y_1, y_2) is the angular position of the source with respect to the optic axis, $m_{\rm s}$ is the apparent r-band magnitude of the source, and $z_{\rm s}$ is the redshift, fixed to $z_{\rm s} = 2$. The angular positions are randomly sampled in the source plane in the vicinity of the caustic structures. We only retain simulated data in which quadruply lensed images are produced in both versions of a given light-cone, i.e. both the single- and the multiple-lens plane version. This reduces our initial selection of 500 light-cones (see Section 3.1) to 400.

With a fully parametrically defined light-cone, the simulated lensed images can be produced by ray tracing and image finding. For our single-lens plane simulations, we determine $\kappa_{\rm ext}$ and $\gamma_{\rm ext}$ in the following manner. First, we trace rays through a given light-cone from the image plane, computing the deflections caused by all haloes (including the primary lens), each in their own lens plane. To obtain $\gamma_{\rm ext}$, along each ray, we compute the cumulative external shear from all haloes. We take $\gamma_{\rm ext}$ to be the median of the distribution of values of the cumulative external shear along different rays in the light-cone. For the external convergence, along each ray, we compute an 'external halo convergence' by summing κ as given by equation (1) for all secondary haloes excluding the primary lens
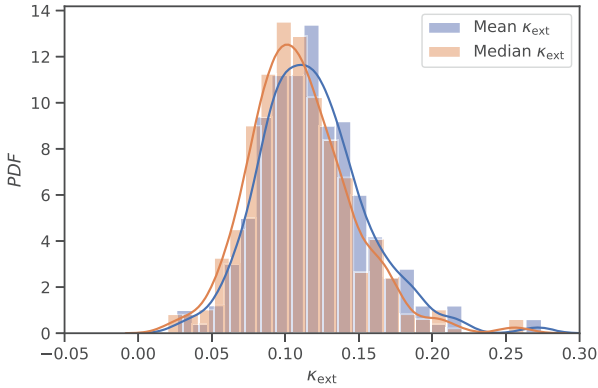
Figure 2. The distribution of the mean (blue) and median (orange) convergence of all fully ray-traced light-cones used in this work. The blue and orange curves show a smoothed version of the distributions calculated using kernel density estimates.

halo. This external halo convergence ignores the divergence caused by voids and so we must apply a correction to obtain κ_{ext}. The correction uses the results of Collett et al. (2013) who showed that κ_{ext} can be obtained by subtracting the median convergence along random sightlines from the external halo convergence. The resulting κ_{ext} has an uncertainty associated with it due to the scatter in the relationship between the two quantities, but negligible bias. Firing rays along random lines of sight in our light-cones and computing the convergence, again using equation (1), yield a value of $\kappa_{corr} = 0.048$. When correcting the external halo convergence, we distribute κ_{corr} across all lens planes according to the lensing weights ($D_{ds}D_d/D_s$) for each plane and subtract them separately.

Fig. 2 shows the probability distribution functions (PDFs) of the mean and median values of κ_{ext} across all light-cones obtained in the manner described. We note that our peak of $\kappa_{ext} \simeq 0.1$ is higher than that of previous studies, for example peaks of 0.075 and 0.05 in Suyu et al. (2013) and McCully et al. (2017), respectively. We attribute this mainly to our selection of BCGs from cosmoDC2 and their location within more overdense galaxy groups. Secondary effects also likely include a difference in mass models and simulated light-cones. Nevertheless, many of our light-cones yield external convergences that are consistent with these studies and so in our analysis, we explore how inferred values of H_0 vary with varying κ_{ext}.

With κ_{ext} determined, we include it in the primary lens model for the single-plane simulations and calculate maps of the deflection angle and the lensing potential. The lensing equation in equation (5) is used to map the image plane back to the source plane. Since the sources in this paper are point sources, we have to adopt a triangle-mapping algorithm to solve the lensing equation. This is described further in Section 3.3.

For the case of multiple-lens planes, we ray trace through the whole light-cone in the same manner as outlined above when computing the external halo convergence, placing each halo on its own lens plane. As equation (20) shows, to calculate the total time delay, the deflection map and lensing potential for every lens plane must be computed. The intersections of the light rays traced from the image plane (given by equation 18) are required for the calculation of the time delay between two lens planes. These are summed over all neighbouring pairs of lens planes to obtain the total time delay according to equation (21). Again, for our adopted point source, we have to apply triangle mapping and barycentric interpolation to obtain the position of lensed images for a given source position on the source

plane (see Section 3.3). The same image-finding process is applied to locate the intersections of the light rays between neighbouring lens planes (see equation 20).

Since we are concerned purely with the effects of line-of-sight structure in this study, we have not included the effects of measurement error in our simulated data, i.e. we do not scatter any of the time delays, image positions, or flux ratios. However, we do use priors in the modelling to allow exploration of parameter degeneracies. More details are given in Section 4.

3.3 Image finding

Since we are concerned with multiply-imaged point-like sources, e.g. active galactic nuclei (AGNs) or SNe, in this work, solving the lensing equation for point sources is a critical issue in the simulation. To determine the apparent positions of our point sources, we make use of a triangle-mapping technique described in (Schneider et al. 1992). First, a set of Delaunay triangles is constructed from a regular grid of image plane positions that define the intersections of light rays from the source (see Fig. 3). These image plane vertices are then mapped to the source plane. Any image plane triangles that map to a triangle in the source plane containing the source position are identified. For each of these identified image-plane triangles, we compute the barycentric coordinate of the source position inside the corresponding source-plane-mapped triangle using the relation

$$\begin{pmatrix} x_1 & x_2 & x_3 \\ y_1 & y_2 & y_3 \\ 1 & 1 & 1 \end{pmatrix} \begin{pmatrix} \lambda_1 \\ \lambda_2 \\ \lambda_3 \end{pmatrix} = \begin{pmatrix} x_P \\ y_P \\ 1 \end{pmatrix}, \qquad (28)$$

where (x_P, y_P) are the Cartesian coordinates of the point source inside its triangle of vertices (x_1, y_1), (x_2, y_2), and (x_3, y_3); the corresponding barycentric coordinates are $(\lambda_1, \lambda_2, \lambda_3)$. We then assume that the barycentric coordinates are conserved between the image and source planes and use them, with the vertices of the image-plane triangle to determine the position of each image of the source.

For the case of multiple-lens planes, the intersections between the light rays from the source and the lens planes are required for the calculation of total time delays. Hence, we need to ascertain all the intersections. If there are N lens planes plus one source plane in the lensing system, there are N parent triangles for the triangle on the source plane. Also, we assume the barycentric coordinates of the source are conserved in the source triangle and all parent triangles. Then the intersections can be obtained. The intersections on the first lens plane (0th plane in Fig. 1) are the positions of the lensed images.

4 STRONG LENS MODELLING

We use the multipurpose open-source lensing package LENSTRONOMY[3] (Birrer, Amara & Refregier 2015; Birrer & Amara 2018) to measure H_0 from our simulated data. For our lens modelling, instead of the SIE profile used to create our simulated data, we use the more general singular elliptical power law (SEPL) profile. The parameters of the SEPL are the Einstein radius, θ_E, the two components of complex ellipticity, e_1 and e_2, the SEPL power-law index, γ, and the coordinates of the SEPL centre (θ_1, θ_2). Also included as free parameters in the modelling are the coordinates of the source (β_1, β_2) in the source plane. Finally, we apply the SEPL model both with and without external shear

---

[3] https://github.com/sibirrer/lenstronomy
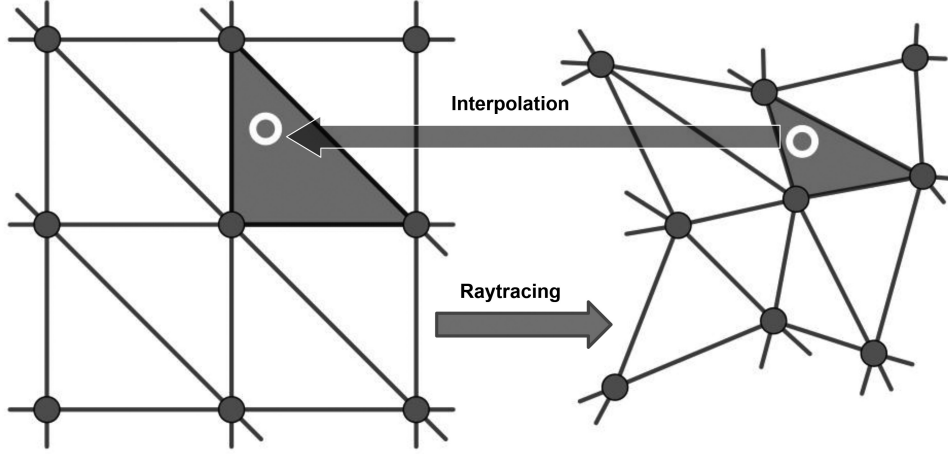
Figure 3. The interpolation scheme used for determining image positions of point sources. The regular grid of rays in the image plane (filled circles in the left-hand panel) is used to partition the image plane into triangles (grey lines in the left-hand panel). The image positions (the open white circle in the left-hand panel) of a source inside a triangle (the grey triangle in the right-hand panel) formed by the backtraced rays on the source plane (grey filled circles in the right-hand panel) are then determined by using linear interpolation in the barycentric coordinates.

Table 1. Uniform priors applied to parameters in the lens modelling.

Model component	Parameter	Prior
Lens, Einstein radius	θ_E (arcsec)	$\mathcal{U}(0.01, 10)$
Lens, power index	γ	$\mathcal{U}(1.7, 2.3)$
Lens, ellipticity	$e_{1,2}$	$\mathcal{U}(-0.5, 0.5)$
Lens, position	$\theta_{1,2}$ (arcsec)	$\mathcal{U}(-10, 10)$
External shear	γ_{ext}	$\mathcal{U}(0.0, 0.5)$
External shear angle	$\theta_{\gamma, ext}$ (rad)	$\mathcal{U}(-\pi, \pi)$
Source, position	$\beta_{1,2}$ (arcsec)	$\mathcal{U}(-10, 10)$
Hubble–Lemaitre constant	H_0 (km s^{-1} Mpc^{-1})	$\mathcal{U}(20, 120)$
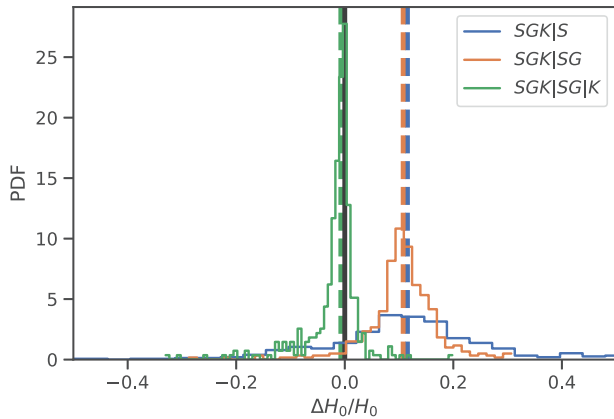
Figure 4. PDFs of the fractional differences between measured H_0 and the true value in the case of the simulations with constant κ_{ext} and γ_{ext}. The blue histogram shows the PDF of fractional differences in H_0 with the single SEPL mass model only. The orange histogram shows the PDF of fractional differences with the mass model of SEPL $+ \gamma_{ext}$, i.e. including external shear as a free parameter. The green histogram shows the corrected fractional differences of the orange histogram with constant κ_{ext} correction. The vertical dashed lines show the median of each PDF, whilst the black vertical solid line is placed at zero bias.

(see below). We use the complex shear parametrized by $\gamma_{ext, 1}$ and $\gamma_{ext, 2}$. We apply generous uniform priors to all model parameters in LENSTRONOMY as detailed in Table 1.

We model all four different combinations arising from the two lens model configurations (i.e. the SEPL with and without external shear) and the two sets of simulated data (i.e. the single- and multiple-lens plane light-cones). We designate the simulations with a single-lens plane as 'SGK' (SIE $+ \gamma_{ext} + \kappa_{ext}$) and those with the multiple-lens plane as 'SL' (SIE + lens planes). Similarly, we designate the lensing model that includes external shear as 'SG' (SEPL $+ \gamma_{ext}$) and that without as 'S'. The four combinations, labelling the simulation type first, are therefore referred to hereafter as 'SGK|S', 'SGK|SG', 'SL|S', and 'SL|SG'. Note that in all cases we fix $\kappa_{ext} = 0$ and retrospectively apply the correction to H_0 for external convergence determined from the simulated light-cones following the procedure used by existing studies (see Section 5). In cases where external shear is not included as a free parameter in the lens model (SGK|S and SL|S), we fix $\gamma_{ext} = 0$.

The simulated data that we fit with LENSTRONOMY are the four image positions, the three flux ratios, and the three time delays. For optimization of the lens model parameters and H_0, we use LENSTRONOMY's particle swarm optimizer (PSO; Kennedy & Eberhart 1995) since this technique performs well in lower dimensional parameter spaces such as ours (see Birrer et al. 2015). We apply the PSO with 200 particles, a particle scatter of 1, and a maximum number of iterations of 500. These choices yield an acceptable computation time whilst still allowing a thorough exploration of the model parameter space.

5 RESULTS

In carrying out the modelling, we find that not all measurements of H_0 obtained are valid. This is due to the limited precision of the simulations; when a source is almost coincident with the caustic in the source plane, the magnifications of the simulated lensed images become unreliable because of the finite image grid size, despite our interpolation. These problematic cases can be effectively removed by imposing a likelihood threshold of $\log(L) > -1000$. This further reduces our sample of 400 lens systems to 364, 372, 366, and 394 lenses in the cases of SGK|S, SGK|SG, SL|S, and SL|SG, respectively. By applying this threshold in likelihood, we also remove poor fits arising from large perturbations from substructures not caught by the 0.3 arcsec cut in Einstein radius.
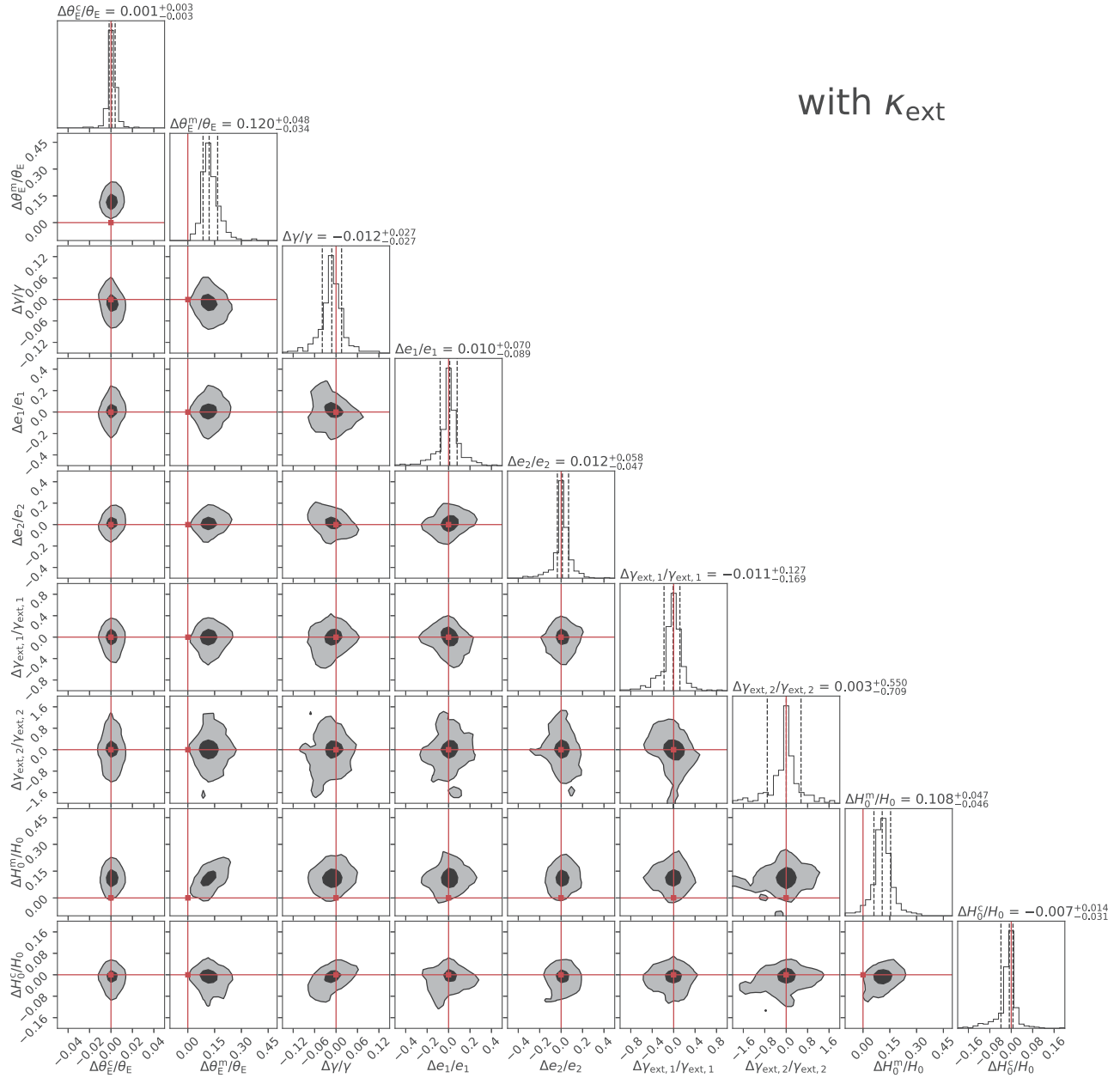
Figure 5. Corner plot showing the distribution of best-fitting parameters of all 372 systems simulated with a single-lens plane and uniform external convergence and shear. The plot includes the Einstein radius and H_0 corrected by the simplistic factor of $1 - \kappa_{ext}$. These are denoted θ_E^c and H_0^c, respectively. γ is the power index of the SEPL mass model, e_1 and e_2 are the two components of the complex ellipticity of lenses, $\gamma_{ext,1}$ and $\gamma_{ext,2}$ are the two components of the complex external shear, H_0^m is the best-fitting uncorrected Hubble constant, and H_0 is the input Hubble constant. The contours show the 1σ and 2σ confidence intervals. The plot is created with CORNER.PY (Foreman-Mackey 2016).

First, we consider our analysis of the simulations created with line-of-sight structure approximated by a constant external convergence and shear. Fig. 4 shows the PDFs of the fractional difference between the input and inferred H_0 obtained for the two different lens models applied, i.e. the SEPL-only model (SGK|S) and the SEPL + γ_{ext} model (SGK|SG). Taking the median of each of these distributions, we find that without including any external convergence in the modelling, the inferred value of H_0 is biased high by $\sim$11 per cent in both cases. The inclusion of external shear in the lens model reduces the spread of the distribution but does nothing to remove the bias.

Following the procedure commonly used in the literature to correct for external convergence effects (see e.g. Suyu et al. 2017), we apply a correction of $1 - \kappa_{ext}$ (with κ_{ext} determined from the simulations as explained in Section 3.2) to the biased measurements of H_0 from the SGK|SG configuration. The green histogram shown in Fig. 4 shows the results of this correction. Clearly, the correction in this simplified case works well, recovering a median value of H_0 that differs from the input value by only -0.7 per cent.

In Fig. 5, we show the two-dimensional probability distributions of all parameter pair combinations for the SGK|SG configuration. Note that in addition to the bias in H_0, there is also a similar bias
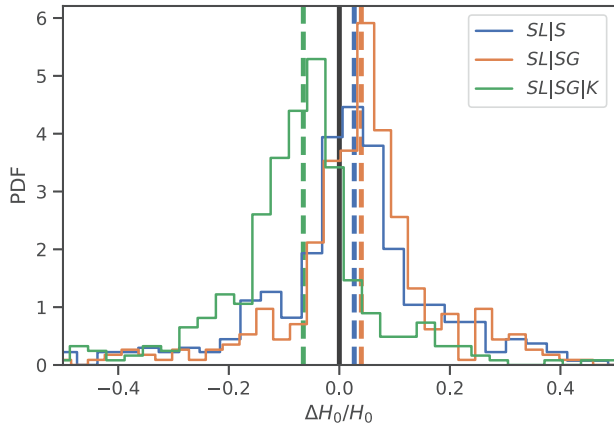
Figure 6. The same as Fig. 4, except using the fully ray-traced simulations containing line-of-sight haloes.

in the inferred Einstein radius, θ_E. This is a result of the strong degeneracy between θ_E and H_0 caused by the fact that the external convergence impacts both quantities by the same factor of $1 - \kappa_{ext}$. As Fig. 5 shows, correcting θ_E by the factor $1 - \kappa_{ext}$ (to give the quantity θ_E^c in the figure), the input value of the Einstein radius is reliably recovered.

Second, we consider our modelling of the simulations created with the full light-cones containing haloes (i.e. the cases of SL|S and SL|SG). Fig. 6 shows the distribution of inferred values of H_0 for both cases. This time, we find that the biases in inferred H_0 are significantly smaller than the biases observed with the single-lens plane light-cones. Now, we find a median value that is 3 per cent and 4 per cent higher than the input value of H_0 for the SL|S and SL|SG cases, respectively. Once again, the inclusion of external shear in the lens model does little to improve the bias. Furthermore, the inclusion of external shear does not reduce the scatter in inferred values of H_0, unlike the single-lens plane modelling. Fig. 6 also shows the histogram of inferred H_0 from the modelling that includes external shear (SL|SG) corrected by $1 - \kappa_{ext}$, where again, κ_{ext} is determined from ray tracing through the light-cone. This time, the correction is too severe and leads to an underestimation of H_0 such that the corrected distribution has a median that is offset by -7 per cent from the input value. We therefore conclude that statistically the $1 - \kappa_{ext}$ correction cannot be reliably used to account for clumpy external convergence.

Similar to Fig. 5, Fig. 7 shows the two-dimensional probability distributions of all parameter pair combinations for the SL|SG configuration. Again, the figure includes both H_0^c and θ_E^c, the inferred values of H_0 and Einstein radius corrected by $1 - \kappa_{ext}$. This time, however, the degeneracy between H_0 and θ_E has been removed by the more complex lens geometry caused by the line-of-sight structure; clumpy external convergence affects the time delays in a different way to the way in which it affects the inferred Einstein radius, unlike when a uniform external convergence is assumed. In the same way that the inferred H_0 is not biased as high with the full light-cones, neither is the inferred Einstein radius and so the correction provided by the factor of $1 - \kappa_{ext}$ is also too severe and also results in a bias of -7 per cent from the input value on average.

Since our simulations span a range of lens systems each with a different median external convergence, κ_{ext}, we can investigate whether there is any correlation between the bias we see in inferred H_0 and κ_{ext}. Identifying such a correlation might instruct future studies on how best to minimize the bias. Fig. 8 shows the scatter

plot of the bias in inferred H_0 versus κ_{ext} for each lens system with the SL|SG configuration. As the figure shows, there is a positive correlation such that the fractional bias in H_0 due to the overcorrection correlates with the median external convergence. The scatter plot can be fitted using a linear function $\Delta H_0/H_0 = 0.626\kappa_{ext} - 0.005$. Unsurprisingly, selecting a lens system in an environment with a stronger level of external convergence is more likely to bias the value of H_0 inferred from that system.

6 DISCUSSION AND CONCLUSIONS

To quantify the influence of secondary deflectors on the measurement of H_0 with strong lensing time delays, we have simulated approximately 800 galaxy-scale strong lensing systems with quadruply lensed variable point sources; half of these were created with a primary lens and line-of-sight haloes and half with the same primary lens plus a constant external convergence and shear. The light-cones were extracted from a semi-analytic model based on the Outer Rim large-scale cosmological simulation and are centred on the location of central galaxies of groups of galaxies. In the simulations constructed with external convergence and shear, we used a single-lens plane located at the redshift of the primary lens galaxy, whereas in the simulations containing haloes, each halo has its own lens plane. Using an SIE mass profile for the primary lens galaxy and the haloes, and an interpolative mapping method to refine the location of the lensed point source images, we generated time-delay data. This time-delay data were then modelled using LENSTRONOMY to estimate H_0 with a singular ellipsoidal power-law lens profile and external shear and compared to the known input value of H_0.

Our main conclusion is that incorporating constant external convergence in the modelling only works reliably if the lensed time delays are subjected to a uniform external convergence. If time delays are subjected to perturbations due to haloes lying close to the line of sight as expected in the real Universe, and no correction for external convergence is made in the modelling, the inferred value of H_0 is overestimated by approximately 4 per cent on average. However, if a constant external convergence is incorporated in the lens model with a normalization set by the median or mean convergence of the line-of-sight haloes, then an overcorrection of H_0 occurs such that it is biased low by ~ 7 per cent on average. These results were obtained from our simulations where we measure a relatively high median external convergence of $\kappa_{ext} \simeq 0.11$ but we find that the size of the fractional bias in H_0 scales almost proportionally with $\kappa_{ext} = 0.11$ on average (see below for details). Nevertheless, even with low levels of external convergence, this effect cannot be ignored, since the uncertainties of current measurements of H_0 from strong lensing time delays are typically quoted as being lower than this (Bonvin et al. 2017; Birrer et al. 2019; Chen et al. 2019; Rusu et al. 2020; Wong et al. 2020). With the forthcoming large sample of strong lensing time-delay systems observed by the future time domain large-scale surveys, e.g. Multichannel Photometric Survey Telescope (Mephisto)[4] and LSST, the effect becomes even more problematic.

Qualitatively, our conclusions are consistent with those of Mc-Cully et al. (2017) in the sense that line-of-sight structures significantly affect the accuracy of the measurement of H_0. We find a larger median external convergence of $\kappa_{ext} \simeq 0.11$ compared to the value of 0.05 from McCully et al. (2017). We attribute this to the fact that

---

[4]http://www.swifar.ynu.edu.cn/info/1015/1073.htm
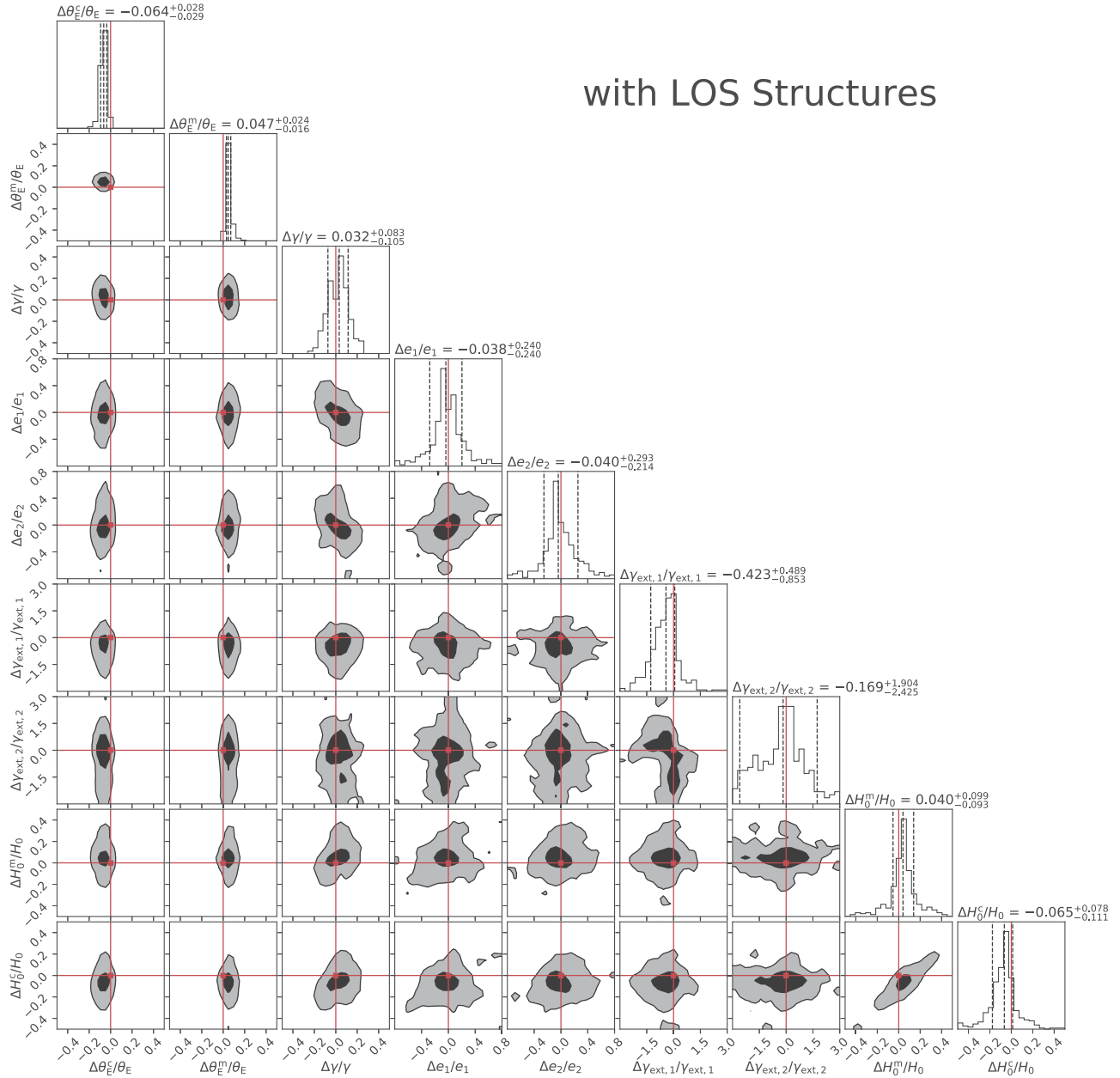
Figure 7. Corner plot showing the distribution of best-fitting parameters of all 394 systems simulated by ray tracing through light-cones containing line-of-sight haloes. All parameters are the same as those in Fig. 5 and the contours again show the 1σ and 2σ confidence intervals.

we have selected central galaxies of galaxy groups as the primary lenses in our light-cones and because we have included more line-of-sight structures; we include galaxies from cosmoDC2 down to an r-band apparent magnitude of 28, compared to the i-band limit of 21.5 adopted by McCully et al. (2017). Nevertheless, our findings indicate that even small values of $\kappa_{\rm ext}$ bias H_0 on average. We have shown that the fractional bias in inferred H_0 correlates with median external convergence according to the linear relationship $\Delta H_0/H_0 = 0.626\kappa_{\rm ext} - 0.005$.

We have also investigated the effects of incorporating external shear in the lens model. In the simulations using line-of-sight haloes, adding an external shear term to the SEPL lens model makes a negligible impact on the distribution of recovered values of H_0. Not unexpectedly, we also find that correcting this SEPL $+ \gamma_{\rm ext}$

model with the average constant external convergence also leads to a $\sim$7 per cent underestimation, which implies that the influence of external shear is negligible in the case of our study. This conclusion differs from that of McCully et al. (2017), most likely because we cleaned our lens sample by removing secondary haloes that give rise to an Einstein radius of greater than 0.3 arcsec.

The Outer Rim simulations used to populate our lensing light-cones with haloes include only dark matter. As such, we have used SIE profiles in place of identified haloes to better represent the total mass (baryons + dark matter) profiles of real lens galaxies. One effect this may have is that the lensing strength of any lower mass haloes, which in the real Universe may not have accrued baryons, could be artificially enhanced by the more efficient isothermal profile. In addition, our simulated data sets do not include any large-scale
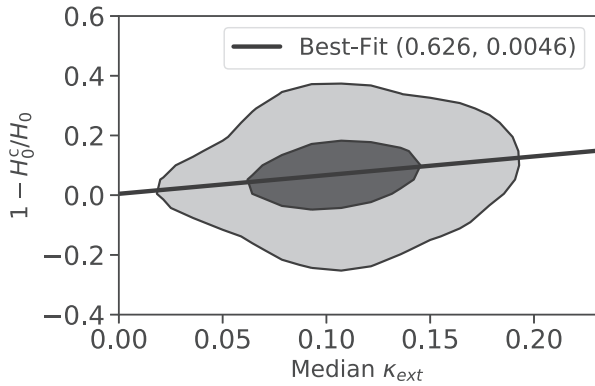
Figure 8. The relationship between the fractional bias seen in the corrected value of H_0, H_0^c, and the median external convergence measured across all 394 fully ray-traced light-cones containing line-of-sight haloes. The contours show the 1σ and 2σ confidence intervals and the black line shows the best-fitting linear relationship that exhibits almost exact proportionality: $1 - H_0^c/H_0 = 0.626\kappa_{ext} - 0.005$.

structure such as filaments, although this is expected to be a small effect. We have explored the use of truncated SIE profiles in place of the non-truncated profiles used in this work but find that our results do not change significantly. Finally, we have ignored the effects of environmental structure in the simulations in the sense that our assumed smooth SIE profiles for the primary lens do not include substructure. We will leave consideration of these additional effects for future work.

To summarize, simple corrections for line-of-sight structure such as external shear or external convergence in estimations of H_0 using lensed time delays cannot be relied upon in general. Time-delay studies opt for lens systems that are apparently free of strong perturbers in an attempt to exclude line-of-sight effects, or they select systems where the perturbers are low in number and can be easily incorporated in the lens model. Our simulations have mimicked the former selection to a degree by removing haloes from all of our light-cones that produce a deflection resulting in an Einstein radius larger than 0.3 arcsec. Since this may still allow a significant flexion shift, an improved technique is to include perturbers in the lens model with a flexion shift above a certain threshold (e.g. Rusu et al. 2020). However, our work reveals that the culmination of many small line-of-sight perturbers continues to result in a significant portion of the measured bias in H_0 and more sophisticated modelling methods, for example, including more lens planes by lowering flexion shift thresholds are key to reliable measurements of H_0 from the hundreds of well-measured time-delay systems anticipated in forthcoming large strong lens samples.

DATA AVAILABILITY

The data underlying this paper will be shared on reasonable request to the corresponding author.

REFERENCES

Addison G. E., Watts D. J., Bennett C. L., Halpern M., Hinshaw G., Weiland J. L., 2018, ApJ, 853, 119
Bennett C. L. et al., 2013, ApJS, 208, 20
Birrer S., Amara A., 2018, Phys. Dark Universe, 22, 189
Birrer S., Amara A., Refregier A., 2015, ApJ, 813, 102
Birrer S., Amara A., Refregier A., 2016, J. Cosmol. Astropart. Phys., 08, 020
Birrer S., Welschen C., Amara A., Refregier A., 2017, J. Cosmol. Astropart. Phys., 04, 049
Birrer S. et al., 2019, MNRAS, 484, 4726
Bolton A. S. et al., 2012, ApJ, 757, 82
Bonvin V. et al., 2017, MNRAS, 465, 4914
Chen G. C. F. et al., 2019, MNRAS, 490, 1743
Collett T. E., 2015, ApJ, 811, 20
Collett T. E., Cunnington S. D., 2016, MNRAS, 462, 3255
Collett T. E. et al., 2013, MNRAS, 432, 679
D'Agostino R., Nunes R. C., 2020, Phys. Rev. D, 101, 103505
DES Collaboration et al., 2020, Phys. Rev. D, 102, 023509
Dhawan S., Jha S. W., Leibundgut B., 2018, A&A, 609, A72
Dobler G., Fassnacht C. D., Treu T., Marshall P., Liao K., Hojjati A., Linder E., Rumbaugh N., 2015, ApJ, 799, 168
Faber S. M. et al., 2007, ApJ, 665, 265
Foreman-Mackey D., 2016, J. Open Source Softw., 1, 24
Freedman W. L. et al., 2019, ApJ, 882, 34
Greene Z. S. et al., 2013, ApJ, 768, 39
Habib S. et al., 2016, New Astron., 42, 49
Heitmann K. et al., 2019, ApJS, 245, 16
Keeton C. R., 2001, preprint (arXiv:astro-ph/0102341)
Kennedy J., Eberhart R. C., 1995, in Proceedings of the IEEE International Conference on Neural Networks. IEEE Service Center, Piscataway, NJ, p. 1942
Koopmans L. V. E., Treu T., Bolton A. S., Burles S., Moustakas L. A., 2006, ApJ, 649, 599
Kormann R., Schneider P., Bartelmann M., 1994, A&A, 284, 285
Korytov D. et al., 2019, ApJS, 245, 26
Li N., Gladders M. D., Rangel E. M., Florian M. K., Bleem L. E., Heitmann K., Habib S., Fasel P., 2016, ApJ, 828, 54
Liao K., et al., 2015, ApJ, 800, 11
Macaulay E. et al., 2019, MNRAS, 486, 2184
McCully C., Keeton C. R., Wong K. C., Zabludoff A. I., 2014, MNRAS, 443, 3631
McCully C., Keeton C. R., Wong K. C., Zabludoff A. I., 2017, ApJ, 836, 141
Momcheva I. G., Williams K. A., Cool R. J., Keeton C. R., Zabludoff A. I., 2015, ApJS, 219, 29
More A. et al., 2016, MNRAS, 455, 1191
Muñoz J. B., Kamionkowski M., 2017, Phys. Rev. D, 96, 103537
Narayan R., Bartelmann M., 1996, preprint (arXiv:astro-ph/9606001)

[5]https://github.com/LSSTDESC/gcr-catalogs

Oguri M., Marshall P. J., 2010, MNRAS, 405, 2579
Parker L. C., Hoekstra H., Hudson M. J., van Waerbeke L., Mellier Y., 2007, ApJ, 669, 21
Pietrzyński G. et al., 2019, Nature, 567, 200
Planck Collaboration VI, 2020, A&A, 641, A6
Riess A. G., 2019, Nat. Rev. Phys., 2, 10
Riess A. G., Casertano S., Yuan W., Macri L. M., Scolnic D., 2019, ApJ, 876, 85
Rusu C. E. et al., 2017, MNRAS, 467, 4220
Rusu C. E. et al., 2020, MNRAS, 498, 1440
Schneider P., Ehlers J., Falco E. E., 1999, Gravitational Lenses, 2nd edn. Springer-Verlag, Berlin
Schneider P., Sluse D., 2013, A&A, 559, A37
Schneider P., Ehlers J., Falco E. E., 1992, Gravitational Lenses. Springer-Verlag, Berlin
Sereno M., Paraficz D., 2014, MNRAS, 437, 600
Shajib A. J. et al., 2020, MNRAS, 494, 6072
Shu Y. et al., 2016, ApJ, 833, 264
Sluse D. et al., 2017, MNRAS, 470, 4838
Suyu S. H., Marshall P. J., Auger M. W., Hilbert S., Blandford R. D., Koopmans L. V. E., Fassnacht C. D., Treu T., 2010, ApJ, 711, 201
Suyu S. H. et al., 2013, ApJ, 766, 70
Suyu S. H. et al., 2017, MNRAS, 468, 2590
Tagore A. S., Barnes D. J., Jackson N., Kay S. T., Schaller M., Schaye J., Theuns T., 2018, MNRAS, 474, 3403
Tie S. S., Kochanek C. S., 2018, MNRAS, 473, 80
Tihonova O. et al., 2018, MNRAS, 477, 5657
Verde L., Treu T., Riess A. G., 2019, Nat. Astron., 3, 891
Wagner J., 2018, A&A, 620, A86
Wertz O., Orthen B., Schneider P., 2018, A&A, 617, A140
Wong K. C., Keeton C. R., Williams K. A., Momcheva I. G., Zabludoff A. I., 2011, ApJ, 726, 84
Wong K. C. et al., 2017, MNRAS, 465, 4895
Wong K. C. et al., 2018, ApJ, 867, 107
Wong K. C. et al., 2020, MNRAS, 498, 1420
Xu D., Sluse D., Schneider P., Springel V., Vogelsberger M., Nelson D., Hernquist L., 2016, MNRAS, 456, 739
Yuan W., Riess A. G., Macri L. M., Casertano S., Scolnic D. M., 2019, ApJ, 886, 61

This paper has been typeset from a TeX/LaTeX file prepared by the author.